Chinese Chemical Letters 36 (2025) 110437

Contents lists available at ScienceDirect

Chinese Chemical Letters

journal homepage: www.elsevier.com/locate/cclet

Amplifying STING activation and immunogenic cell death by metal-polyphenol coordinated nanomedicines for enhanced cancer immunotherapy

Yanjun Cai[a,1], Yong Jiang[a,1], Yu Chen[a,1], Erzhuo Cheng[a], Yuan Gu[a], Yuwei Li[a], Qianqian Liu[a], Jian Zhang[a], Jifang Liu[b,*], Shisong Han[c,*], Bin Yang[a,b,*]

[a] The Fourth Affiliated Hospital of Guangzhou Medical University, School of Biomedical Engineering, Guangzhou Medical University, Guangzhou 511436, China

[b] The Affiliated Qingyuan Hospital (Qingyuan People's Hospital), Guangzhou Medical University, Qingyuan 511518, China

[c] Zhuhai Institute of Translational Medicine, Guangdong Provincial Key Laboratory of Tumor Interventional Diagnosis and Treatment, Zhuhai People's Hospital (Zhuhai Clinical Medical College of Jinan University), Zhuhai 519000, China

ARTICLE INFO

Article history:
Received 22 July 2024
Revised 4 September 2024
Accepted 9 September 2024
Available online 10 September 2024

Keywords:
Immunotherapy
STING activation
Ferroptosis
Immunogenic cell death
Metal-polyphenol nanomedicines

ABSTRACT

Ferroptosis in combination with immune therapy emerges as a promising approach for cancer therapy. Herein, dual-responsive metal-polyphenol coordinated nanomedicines were developed for pH/glutathione (GSH)-responsive synergistic ferroptosis and immunotherapy. Our innovative strategy involves the development of a manganese-polyphenol coordinated nanostructure, leveraging the biocompatibility of bovine serum albumin (BSA) as a template to encapsulate the anticancer drug sorafenib. The tumor microenvironment (pH/GSH) prompts the disassembly of MnO_2 and epigallocatechin gallate (EGCG), thereby releases the anticancer payload. Concurrently, MnO_2 acts to deplete intracellular GSH, which in turn suppresses glutathione peroxidase activity, leading to an accumulation of lipid peroxides with cell ferroptosis. Additionally, the release of Mn^{2+} ions bolster the cyclic guanosine monophosphlic acid (GMP)-adenosine monophosphlic acid (AMP) synthase-stimulator of interferon gene (cGAS-STING) pathway, which, in conjunction with the immunogenic cell death (ICD) effect induced by tumor cell apoptosis, significantly promotes dendritic cell (DC) maturation and enhances the presentation of tumor antigens. This successively ignites a robust innate and adaptive immune response. Both *in vitro* and *in vivo* experiments have demonstrated that the concurrent administration of ferroptosis-inducing and immune-stimulating therapies can significantly inhibit tumor growth.

© 2025 Published by Elsevier B.V. on behalf of Chinese Chemical Society and Institute of Materia Medica, Chinese Academy of Medical Sciences.

Since the concept of ferroptosis was proposed in 2012, research in this field has deepened significantly over the years. This distinctive mode of cell death is characterized by iron-dependent phospholipid peroxidation [1,2]. It was worth noting that drug-resistant cancer cells, especially those in the interstitial state and easy to metastasize, are prone to ferroptosis. Various antioxidant systems, especially Xc-glutathione-glutathione peroxidase 4 (GPX4) system, play an import role in preventing lipid peroxidation mediated ferroptosis [3]. The depletion of glutathione (GSH) leads to the inactivation of GSH peroxidase [4,5]. Lipid peroxidation was also a sign of ferroptosis [6,7]. However, ferroptosis injury could trigger inflammation related immunosuppression in the tumor microenvironment (TME), which paradoxically promotes tumor growth [8]. In response, the concept of tumor immunotherapy has emerged, aiming to restore or enhance the functionality of $CD8^+$ T cells in the tumor microenvironment. Immunotherapy-activated $CD8^+$ T cells can enhance the specific lipid peroxidation associated with ferroptosis in tumor cells, thereby augmenting the anti-tumor efficacy of immunotherapy [9]. At the same time, tumor cells with ferroptosis released damage-associated molecular pattern (DAMP) signals through high-mobility group box 1 (HMGB1) emission and calreticulin (CRT) translocation to the surface of cells. The release of these "eat me" signals could promote dendritic cells (DCs) maturation, thereby activating antitumor immunity [10-12]. DCs are hematopoietic cells specialized in capturing, processing, and presenting antigens to T cells, they also play a pivotal role in innate immune function. Consequently, DCs are recruited to process

* Corresponding authors.
E-mail addresses: yzhbb2012@126.com (J. Liu), hanshs@qq.com (S. Han), bin.yang@gzhmu.edu.cn (B. Yang).

[1] These authors contributed equally to this work.

https://doi.org/10.1016/j.cclet.2024.110437
1001-8417/© 2025 Published by Elsevier B.V. on behalf of Chinese Chemical Society and Institute of Materia Medica, Chinese Academy of Medical Sciences.

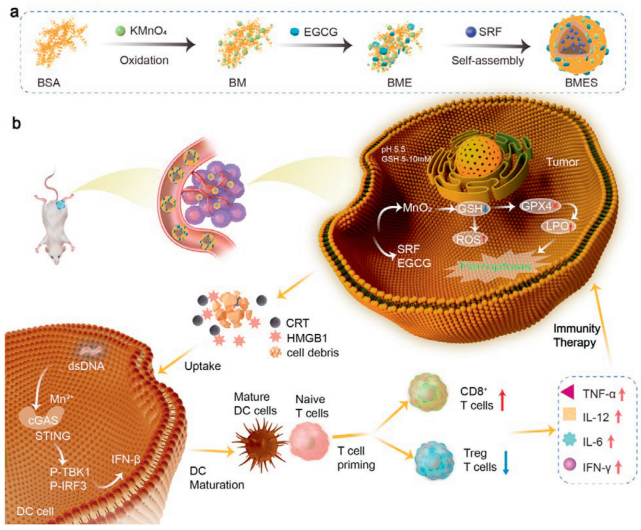

Scheme 1. (a) Schematic illustration of the synthesis of metal-polyphenol coordinated nanomedicines. (b) Schematic illustration of the stimulating dual-response ferroptosis in combination with STING pathway-dependent immune therapy.

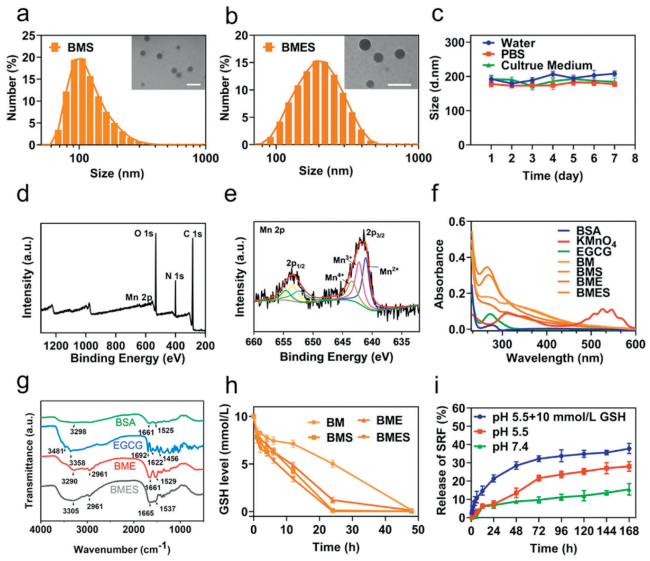

Fig. 1. Characterizations of nanomedicines. (a) Size distribution of BMS NPs determined by dynamic light scattering. Transmission electron microscopy image of BMS NPs is inserted. (b) Size distribution of BMES NPs determined by dynamic light scattering. Transmission electron microscopy image of BMES NPs is inserted. Scale bar: 200 nm. (c) Size variations of BMES NPs under different conditions during 7 days ($n = 3$). (d) XPS spectra of BMES NPs. (e) Mn 2p high-resolution XPS spectrum of BMES NPs. (f) The ultraviolet-visible (UV–vis) absorption spectra of BSA, $KMnO_4$, EGCG, BM, BMS, BME and BMES NPs. (g) The FTIR spectra of BSA, EGCG, BME and BMES NPs. (h) The level of GSH measured by recording absorption intensity of DNTB at 412 nm in BM, BME, BMS and BMES NPs ($n = 3$). (i) SRF release profile of BMES under different conditions ($n = 3$). Data are presented as mean ± standard deviation (SD).

tumor-associated antigens (TAAs) and initiate the tumor immune cycle involving cytotoxic T lymphocytes [13-15].

The stimulator of interferon gene (STING) pathway is a vital component of the cytosolic DNA-sensing mechanism. When aberrant cytosolic DNA binds to cGAS [cyclic guanosine monophosphlic acid (GMP)-adenosine monophosphlic acid (AMP) (cGAMP) synthase], it is detectable in the cell, and cGAS produces cGAMP, which in turn engages and activates the STING pathway [16]. Signaling downstream of STING leads to type I interferon (IFN) production, activation of antigen-presenting cell (APC) and production of inflammatory cytokines, which subsequently promote T-cell priming [17]. Exogenous agonists of STING pathway may have the potential to trigger innate immune activation, leading to adaptive immune response, which is a potential immunotherapy method [18,19]. However, traditional STING agonists, such as cyclic dinucleotides (CDNs), have limited their clinical application due to their inherent properties and low metabolic stability [20]. Recent studies have shown that Mn^{2+} acts as an adjuvant to directly activate cGAS and increase the binding affinity of cGAMP-STING. It recognized the sensitivity of tumor-derived DNA in DCs and stimulated the production of type I IFN to promote the maturation of DCs [21-23]. Therefore, Mn-based STING agonists were therefore a promising strategy to activate the robust anticancer immune response *in vivo*.

Metal coordination platforms have special physicochemical properties which can exploit the advantages of conventional inorganic and organic materials [24-26]. Herein, we employed dual-stimulus-responsive manganese-polyphenol based coordination nanostructures to synergize ferroptosis with immunotherapy, thereby curtailing tumor growth. This innovative approach has paved the way for the development of responsive nanocomposites in the field of cancer therapy. Using bovine serum albumin (BSA) as a template, a layer of MnO_2 nanosheets was grown by *in situ* reduction of $KMnO_4$ [27,28]. The polyphenol epigallocatechin gallate (EGCG) was prepared by non-covalent reaction with BSA and by catechol metal coordination reaction with Mn^{2+} ions [29] to further coat sorafenib (SRF) (Scheme 1) [30]. In the presence of GSH and H^+, the MnO_2 nanoparticles (NPs) in the nanoplatform could be rapidly degraded, achieving the sudden release of Mn^{2+} from the nanoplatform in the TME [31]. After systemic injection of BSA-MnO_x-EGCG-SRF (BMES) NPs into mice bearing 4T1 tumors, the breakdown of MnO_2 led to the release of SRF, Mn^{2+} and EGCG. MnO_2 could deplete intracellular GSH to inhibit the activity of GSH peroxidase, leading to the accumulation of lipid peroxides, which triggers cell ferroptosis. Additionally, SRF and EGCG contribute to the destruction of tumor cells. The resulting cell debris and dying cells release DAMPs to mature immature DCs and initiate adaptive immune response. Together with the *in-situ* release of Mn^{2+} in the TME to activate the cGAS-STING pathway, demonstrating the potential for efficient DCs maturation. Furthermore, mature DCs mediate robust antitumor immune responses, including cross-presentation of tumor antigens and priming of cytotoxic T cells. In summary, unlike previous reports that Mn-based nanomaterials only provided an adjunctive function of GSH consumption in tumor therapy, rationally designed Mn-based nanomaterials could directly induce ferroptosis and activate autoimmunity both *in vitro* and *in vivo*, achieving efficient tumor therapy.

Owing to the excellent biocompatibility of BSA and the strong oxidability of $KMnO_4$, the synthesis of BSA-MnO_x-SRF (BMS) was briefly based on the redox reaction between BSA and $KMnO_4$, in which antitumor drug SRF was self-assembled into the MnO_x to obtain the BMS NPs. For the synthesis of BMES NPs, EGCG, a tea-derived polyphenol was responded with excess BSA through the noncovalent interaction and coordinated with Mn^{2+} ions *via* a catechol-metal coordination interaction. The coordination structure between polyphenols and metal ions was a pH-sensitive process so that it could be destroyed by the weakly acidic microenvironment in the tumor cells to realize the release of EGCG and SRF. As shown in Fig. 1a, the size of BMS is 106 ± 5 nm through dynamic light scattering while the transmission electron microscope (TEM) image inserted showed that BMS possessed a spherical morphology with the size of about 60 nm. The hydrodynamic size of BMES NPs (Fig. 1b) is slightly higher than the BMS NPs, the dynamic size is 190 ± 10 nm while the TEM image inserted showed that BMES possessed a spherical morphology with the size of about 100 nm.

The change of particle size and polydispersity indexes of BMS and BMES during 7 days were studied by dynamic light scattering, and the results showed that the particle size under different conditions was consistent with that in water (Fig. 1c and Fig. S1 in Supporting information). Surface analysis of BMES was carried out using X-ray photoelectron spectroscopy (XPS, Fig. 1d). The Mn 2p spectrum exhibited two contributions, $2p_{1/2}$ and $2p_{3/2}$ (resulting from the spin-orbit splitting) (Fig. 1e). The $2p_{3/2}$ peak in the XPS data can be divided into three characteristic peaks at 640.8, 641.7, and 642.8 eV, each of which corresponds to the reported valence state values of MnO, Mn_2O_3, and MnO_2 respectively, indicating the presence of Mn(II), Mn(III) and Mn(IV). As shown in Fig. 1f, the increased absorbance of BMS and BMES relative to BM and BME at 265 nm suggests the loading of SRF. The characteristic absorption peak between 3200 and 3500 cm^{-1} was caused by tensile vibration of the O–H bond, and the characteristic absorption peak of BSA is located at 3298 cm^{-1}. However, in the spectra of the BME and BMES complexes, the characteristic absorption peaks shifted to 3290 and 3305 cm^{-1}, respectively, indicating a hydrogen bond interaction between EGCG and BSA. In addition, absorption peaks at 1661 and 1542 cm^{-1} were observed in BSA, which were associated with the amide I (C=O stretching) and II (bending vibration of the N–H group and C–N stretching) bands, respectively. However, in the BMES complex, the corresponding absorption peaks were located at 1665 and 1537 cm^{-1}, which were attributed to the electrostatic interaction between BSA and EGCG, indicating the successful synthesis of BMES (Fig. 1g). Since overexpressed GSH in cancer cells can degrade MnO_2 to Mn^{2+}, different nanoparticles were placed with GSH at a concentration of 10 mmol/L, mimicking the activation of these nanoparticles in the tumor microenvironment (Fig. 1h). As expected, GSH breaks down the MnO_2 outer layer of different nanoparticles. The degradation of GSH in reaction with BMES relative to other NPs was the fastest. The rate of SRF release from BMES was studied under different conditions (Fig. 1i). The results showed that SRF was released at pH 5.5 with 10 mmol/L GSH at a fastest rate, which is similar to the tumor microenvironment and endocytosis environment. The metal coordination ability of EGCG varied at different pH values, and the weak stability in acidic environment accelerated the degradation of nanoparticles.

The cytotoxicity of different nanoparticles was detected in breast cancer cells compared to free SRF (Fig. 2a). BMS and BMES exhibit higher toxicity in 4T1 cells compared to free drugs. According to Figs. S2–S5 (Supporting information), although the SRF concentration of BMS and BMES was the same, the concentration of Mn in BMES was less than in BMS, which could speculate that EGCG might also played a role in antitumor. To figure out how these particles induce cell death, a ferroptosis inhibitor, Fer-1, was used to co-culture cells with BMS and BMES groups, cell viability was partially restored after Fer-1 treatment (Fig. 2b). These results suggested that the nanoparticles induced cell death through ferroptosis. As the overexpressed GSH in cancer cells could degrade MnO_2 into Mn^{2+}, GSH was used to co-culture cells with BMS and BMES groups, cell viability was partially restored after GSH treatment (Fig. 2c). The intracellular uptake of BMES NPs was detected by flow cytometry (Fig. 2d), which showed that the uptake of BMES were increased as the time increasing. Ferroptosis was mainly reflected in the changes in the morphological characteristics of mitochondria, which could be observed that a large amount of reactive oxygen species (ROS) will be deposited in the cells [32,33]. An important cause of cell damage was oxidative damage, and mitochondria played an important role in the process of ROS generation and scavenging. The cellular antioxidant capacity is reduced and ROS was generated, which would aggravate mitochondrial dysfunction and hinder GSH absorption [34]. Then GSH deficiency in turn reduced GPX4 activity. Furthermore, the loss of GPX4 directly lead to the occurrence of ferroptosis, which could play an anti-tumor role in tumor cells. To investigate the ROS generation, we utilized 2′,7′-dichlorodihydrofluorescein diacetate (DCFH-DA), a widely recognized and reliable probe for detecting ROS. This compound is susceptible to oxidation by free radicals, which subsequently leads to the formation of 2′,7′-dichlorofluorescein (DCF). The resulting DCF exhibits a distinct green fluorescence, thereby providing a visual and measurable indication of ROS activity. As shown in Fig. 2e, the production of ROS generated by the BMS, BSA-MnO_x-EGCG (BME) and BMES were significantly elevated. As GPX4 could be used as one of the indicators of ferroptosis, the expression of GPX4 was detected in 4T1 cells after different treatment. As shown in Figs. 2f and g, SRF and BM can slightly down-regulate GPX4 expression while BME and BMES show stronger suppressive effect. The GPX4 activity detected by the total glutathione peroxidase assay kit with NADPH and ATP Assay Kit also came to the same conclusion (Fig. 2h).

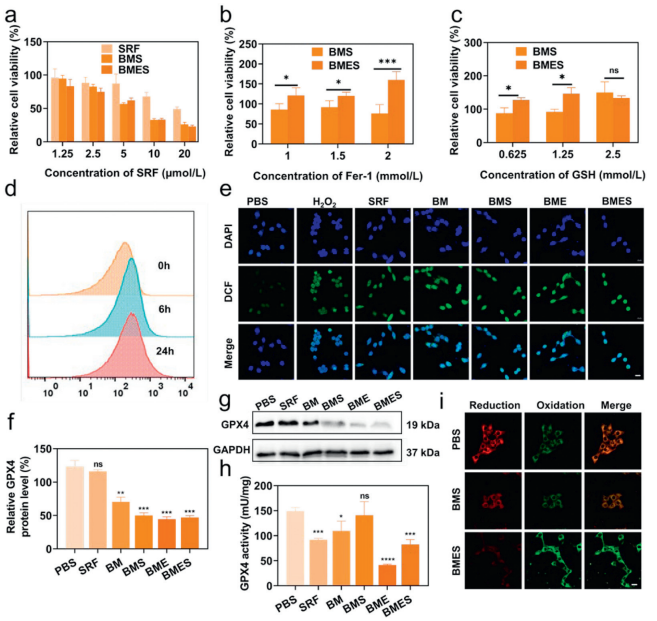

Fig. 2. *In vitro* therapeutic efficacy. (a) Cytotoxicity of SRF, BMS and BMES NPs according to the concentration of SRF in 4T1 cells for 24 h. (b) Relative viability of 4T1 cells after incubation with BMS and BMES NPs at the presence of Fer-1 for 24 h. (c) Relative viability of 4T1 cells after incubation with BMS and BMES at the presence of GSH for 24 h. (d) Flow cytometry result of intracellular uptake of BMES NPs in 4T1 cells at different time. (e) CLSM images of DCFH-DA assay in 4T1 cells detecting intracellular ROS level with different treatment. The 4′,6-diamidino-2-phenylindole (DAPI) staining (blue) was used to label cell nuclei. (f, g) Expression and quantitative analyses of GPX4 in 4T1 cells with different treatment for 24 h. (h) Detection of the GPX4 activity in 4T1 cells after treating different NPs. (i) CLSM images of $BODIPY^{581/591}$-C11 assay in 4T1 cells detecting mitochondrial membrane potential with different treatment. Scale bar: 20 μm. $^{*}P < 0.05$, $^{**}P < 0.01$, $^{***}P < 0.001$, $^{****}P < 0.0001$ were tested *via* a Student's *t*-test with the comparison of PBS and other groups. ns, none significance. Data are presented as mean ± SD ($n = 4$).

The ROS production could not remain in cell forever, it further attacked polyunsaturated fatty acids in the mitochondrial membrane by producing lipid peroxides, resulting in mitochondrial membrane dysfunction. $BODIPY^{581/591}$-C11 was used to detect the presence of lipid peroxides because its excitation wavelength changes when oxidized by lipid peroxides, which can be observed by confocal microscopy. In Fig. 2i, the prevalence of green fluorescence in cells treated with BMES indicated highest level of lipid peroxides in these groups. The lipophilic $BODIPY^{581/591}$-C11 probe was highly sensitive to oxidation and green fluorescence indicated high concentrations of ROS in cells, especially in cell membranes.

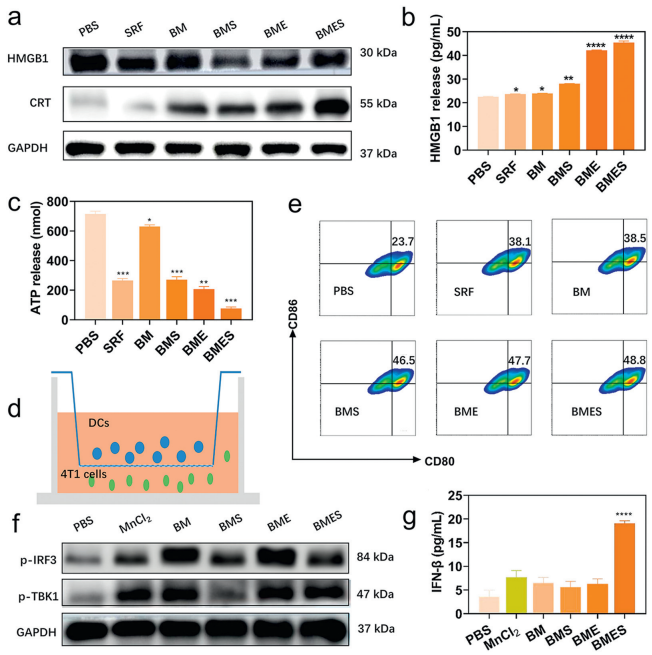

Fig. 3. *In vitro* promotion of DCs maturation. (a) Expression of HMGB1 and CRT in 4T1 cells with different treatment for 24 h by Western blot. (b) ELISA analysis of HMGB1 released from 4T1 cells with different treatment for 24 h. (c) ATP level of the medium culture in 4T1 cells was detected with different treatment for 24 h. (d) Schematic of the transwell chamber for cell co-culture. (e) Flow cytometric analyses of mature DCs ($CD80^+$ $CD86^+$). (f) The activation of cGAS-STING pathway in DCs co-cultured in 4T1 cells with different treatment by Western blot. Glyceraldehyde-3-phosphate dehydrogenase (GAPDH) is used as a reference protein to standardize protein expression levels. (g) The production of IFN-β evaluated by ELISA with different treatment. $^*P < 0.05$, $^{**}P < 0.01$, $^{***}P < 0.001$, $^{****}P < 0.0001$ were tested *via* a Student's *t*-test with the comparison of PBS and BMES groups. Data are presented as mean ± SD ($n = 4$).

Large amounts of ROS tend to attack unsaturated fats in cell membranes and form lipid peroxides.

When tumor cells succumb to external stimuli, such as ferroptosis, they undergo a pivotal transformation from a non-immunogenic to an immunogenic state. This transition is instrumental in triggering an anti-tumor immune response. The phenomenon where cell death becomes capable of eliciting such an immune reaction is known as immunogenic cell death (ICD) [35]. DAMPs released during ICD such as CRT, HMGB1 and ATP molecules could bind to pattern recognition receptors (PRRs) on the surface of DCs and initiate a series of cellular responses, which ultimately activate innate and adaptive immunity [36-38]. In order to evaluate whether ICD occurred, the expression of CRT and HMGB1 in 4T1 cells treated with different materials was detected by Western blot analyses. As shown in Fig. 3a and Fig. S6 (Supporting information), the expression of CRT in BMES treatment was the most and it could be concluded that CRT would translocate and be exposed to the surface of the cell membrane, releasing an "eat-me" signal to immune cells and activating the immune response of the body. The expression of HMGB1 was not only measured by Western blot analysis but also detected using enzyme-linked immunosorbent assay (ELISA) (Figs. 3a and b; Fig. S7 in Supporting information). Although Western blot analysis did not reveal any significant differences, ELISA results showed the highest release of HMGB1 with BMES treatment. The intracellular ATP levels were decreased (Fig. 3c) indicating ATP was released outside the cell with the “find-me” signal and promote the differentiation of immature dendritic cells (DCs) into mature DCs, thereby performing the function of antigen presentation. A schematic representation of the transwell chamber is shown in Fig. 3d. In order to verify the immune activation effect of NPs, 4T1 cells were treated with different NPs for 24 h, then co-cultured with dendritic cells from mouse bone marrow (BMDCs) in transwell chamber for 24 h, and detected the maturation of DCs with flow cytometry. The results showed that in the co-culture system of tumor cells pretreated with BMES, the proportion of mature DCs reached 48.8% (Fig. 3e). The above results indicate that BMES can induce DCs to mature and produce anti-tumor immune effects.

Mn^{2+} can activate the cGAS-STING pathway and increase the sensitivity of cGAS to damaged DNA, resulting in the body's autoimmune effect [39,40]. Thus, manganese containing NPs could be internalized by 4T1 cells to react with GSH and release Mn^{2+}. In this way, damaged DNA fragments in DCs can be more easily sensed by the cGAS enzyme, thereby activating the cGAS-STING pathway for antitumor immunity. To prove this theory, 4T1 cells were firstly treated with different materials for 24 h, then DCs were co-cultured with the treated 4T1 cells in a transwell chamber and proteins of DCs were further collected for evaluation of protein expression in the cGAS-STING pathway. Western blot results showed that NPs promoted the upregulation of phosphorylated tank-binding kinase 1 (p-TBK1) and phosphorylated interferon regulatory factor 3 (p-IRF3) proteins (Fig. 3f, Fig. S8 in Supporting information). Interferon beta (IFN-β) is a kind of type I interferon. It is reported that STING activation results in the activation of TBK1, phosphorylation of IRF-3, and production of type I interferons, which trigger tumor antigen cross-presentation and antitumor T cell immune responses. The production of IFN-β was evaluated by ELISA, and the results were shown in Fig. 3g. IFN-β secreted by BMDC in the BMES group was higher than that of the control group and other experimental groups, further indicating that BMES activated the cGAS-STING pathway.

To evaluate the *in vivo* antitumor therapeutic effect of nanomedicines, the 4T-1 tumor-bearing model was selected. All animal procedures abided by the criterion of the Institutional Animal Care and Use Committee (IACUC) of the Animal Experiment Center of Guangzhou Medical University (Guangzhou, China) and were performed following institutional approval (GY2021-048). When the tumor volume reached about 100 mm^3, the mice were randomly divided into 6 groups and injected intravenously with 100 μL phosphate buffered saline (PBS), $MnCl_2$, free SRF, BM, BMS and BMES. As shown in Fig. 4a, the nanomedicines (based on Mn at 2.5 mg/kg) were injected intravenously twice every other day. The weight and volume of the primary tumor was monitored every two days during treatment. At the end of the treatment, major organs, tumor tissue and blood samples were collected from the mice for subsequent experiments. The tumors were photographed (Fig. 4b) and weighed (Fig. S9 in Supporting information). Compared with PBS group, free SRF showed little anticancer effect. Manganese chloride was good at the beginning of treatment, but later the treatment effect became worse probably because manganese chloride stayed in the body for a short time. However, BMES showed the best inhibitory effect on tumor growth. On day 14, the relative tumor volume in the BMES group was significantly lower than that in other groups (Fig. 4c), reflecting a slower tumor growth rate. This proved that BMES nanomedicine has the best anti-tumor effect. As shown in Fig. 4d, the stable body weight curves showed there was negligibly significant difference in body weights among these groups because of no systemic toxicity after different treatments. The main organs and tumors from the mice were stained with hematoxylin and eosin (H&E). The outcome indicated that the treatment did not cause heart, liver, spleen, lung and kidney injure (Fig. S10 in Supporting information). Terminal deoxynucleotidyl transferase dUTP nick end labeling (TUNEL) staining was also performed, and tumor cells from the BMES group were found to be highly apoptotic compared with controls (Fig. 4e, Fig. S11 in Supporting information). Tumors were also stained

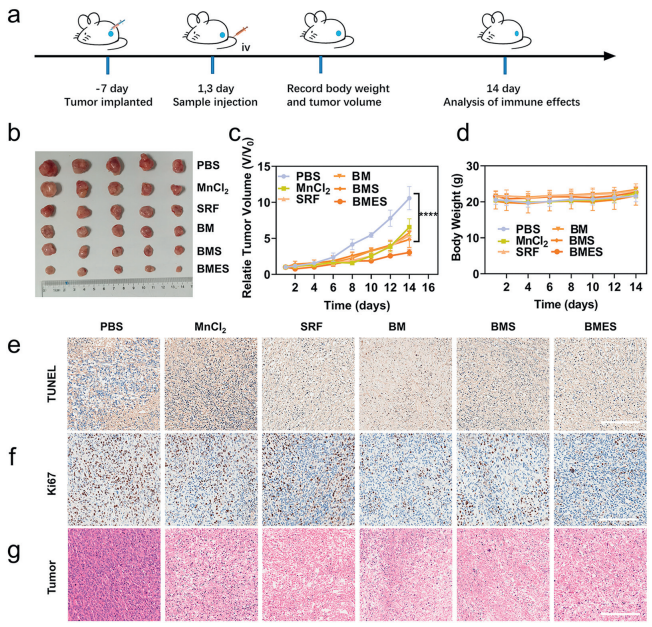

Fig. 4. *In vivo* therapeutic effect of tumor. (a) Scheme illustrated the experimental steps for breast cancer mice model. (b) Images of 4T1 tumors after treatment from different groups. (c) Relative tumor volume change in different groups. (d) The body weight of mice during different treatments. (e) TUNEL staining of 4T1 tumors from different groups. (f) Ki67 staining of 4T1 tumors from different groups. (g) H&E staining of 4T1 tumors from different groups. Scale bar: 200 μm. $^{****}P < 0.0001$ was tested *via* a Student's *t*-test. Data are presented as mean ± SD ($n = 5$).

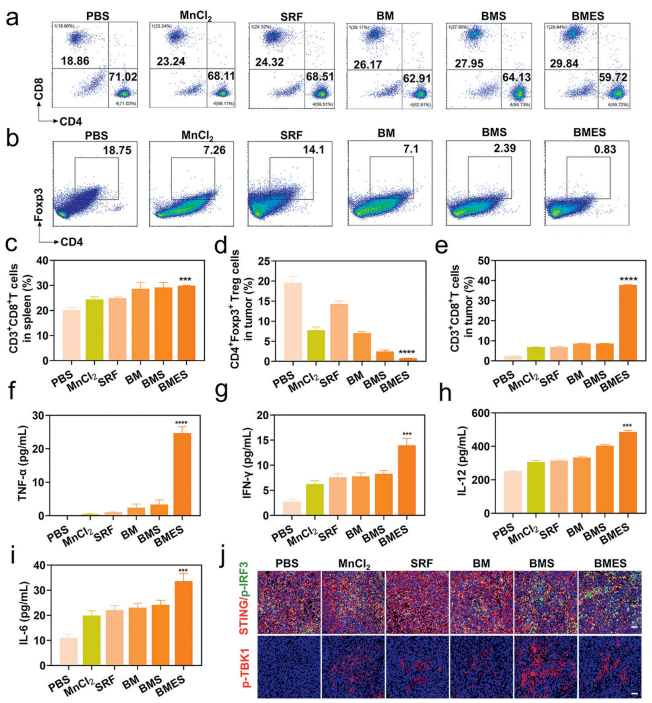

Fig. 5. *In vivo* antitumor immune response of metal-polyphenol coordinated nanomedicine. (a, c) Flow cytometry and quantitative analyses of $CD4^+$ T cells and $CD8^+$ T cells in spleen. (b, d) Flow cytometry and quantitative analyses of $CD4^+$ $Foxp3^+$ Treg cells in tumors. (e) Quantitative analyses of flow cytometry of $CD8^+$ T cells in tumors. (f–i) ELISA analysis of TNF-α, IFN-γ, IL-12, IL-6 in serum from mice. (j) Immunofluorescence staining of tumor tissues. The cell nucleus is shown in blue, p-IRF3 in green, STING in red, and p-TBK1 in red. Scale bar: 50 μm. $^{***}P < 0.001$, $^{****}P < 0.0001$ were tested *via* a Student's *t*-test with the comparison of PBS and BMES groups. Data are presented as mean ± SD ($n = 5$).

by Ki67 and BMES group was the most effective in inhibiting cell proliferation (Fig. 4f, Fig. S12 in Supporting information). The H&E staining of tumors (Fig. 4g) investigated the growth inhibition and severe histological damages. To further evaluate the biosafety of the nanomedicines, blood samples collected from mice were used for blood routine and blood biochemical analysis (Fig. S13 in Supporting information). The physical indicators were almost identical within the all groups so that there was almost no liver or kidney damage.

As reported that Mn^{2+} could increase the sensitivity of cGAS to dsDNA and promote the activation of STING [41], then activate the body's autoimmune effect, so that BMES nanomedicines might be involved in the induction of anti-tumor immune response. The population of effector T cells (including $CD8^+$ T cells and $CD4^+$ T cells) in the spleens and tumors were determined by flow cytometry (Figs. 5a, c and e). Compared with PBS group, BMES group significantly enhanced the infiltration of cytotoxic T cells, and made the number of $CD8^+$ T cells and $CD4^+$ T cells reach about 29.84% and 59.72%, respectively, indicating a stronger upregulation in splenic T cells. Generally, as one of the reasons for poor prognosis of clinical tumor patients, the infiltration of regulatory T cells (Tregs) in TME is an important indicator. Therefore, Tregs ($CD4^+$, $CD25^+$ and $Foxp3^+$) in the tumor site were detected by flow cytometry (Figs. 5b and d). PBS group showed up to 19.5% ± 2.0% Treg infiltration, indicating that tumors with poor immunogenicity could recruit Tregs into TME. While the frequency of Tregs in the SRF group decreased slightly by 1.36-fold. On the contrary, the frequency of Tregs in BMES group decreased by an incredible 21-fold. In addition, immune cytokines in serum were detected by ELISA. Treatment with BMES resulted in significant increase in tumor necrosis factor-α (TNF-α), IFN-γ, interleukin-6 (IL-6), and IL-12 compared to all other treatments, suggesting effective cellular immune responses were induced (Figs. 5f–i).

The cGAS-STING pathway activates tumor specific $CD8^+$ T cells by producing type I interferon, enhances the cross presentation of DCs, and finally produces anti-tumor immunity. In order to further study the role of nanomedicines in activating the immune system, we collected the tumor tissues of mice treated with different groups and tested the relevant immune indicators. STING (red), p-IRF3 (green) and p-TBK1 (red) immunofluorescence staining were performed in tumor tissues. The results showed that the p-IRF3 and p-TBK1 fluorescence intensity in tumor tissue slices of mice treated with BMES was the highest, indicating that BMES increased the expression of cGAS-STING related proteins in tumor tissues (Fig. 5j). The above results confirmed that BMES could produce high anti-tumor immune response by activating STING pathway.

In conclusion, we have successfully designed and validated manganese-polyphenol-based nanostructures, known as BMES, as potent therapeutic nanoplatforms. These nanoplatforms are adept at synergistically combining the therapeutic effects of ferroptosis with immunotherapy. The BMES nanostructures were synthesized using BSA as a template. This design leverages BSA's biocompatibility to encapsulate the anti-tumor drug sorafenib, facilitating targeted drug delivery and release under dual stimulus conditions of pH and GSH. The innovative aspect of BMES lies in its ability to release both anti-tumor drug and MnO_2 in response to TME. Within this environment, MnO_2 is reduced to Mn^{2+} by GSH, which not only depletes GSH, leading to ROS accumulation, but also activates the cGAS-STING pathway. The activation enhances the cytosolic dsDNA recognition potential of DCs, further augmenting the immune response. BMES have demonstrated significant efficacy in amplifying STING activation, ICD and ferroptosis. These combined effects not only lead to the destruction of tumor cells but also trigger robust cellular immune responses. Our findings underscore the potential of this strategy to enhance the therapeutic effects of both

ferroptosis and immunotherapy, offering a promising approach for efficient anti-tumor therapy.

Declaration of competing interest

The authors declare that they have no known competing financial interests or personal relationships that could have appeared to influence the work reported in this paper.

CRediT authorship contribution statement

Yanjun Cai: Writing – original draft, Validation, Resources, Methodology, Investigation, Formal analysis, Data curation, Conceptualization. **Yong Jiang:** Visualization, Validation, Software, Resources, Methodology. **Yu Chen:** Validation, Software, Methodology, Investigation, Data curation. **Erzhuo Cheng:** Visualization, Resources, Data curation. **Yuan Gu:** Methodology, Formal analysis, Data curation. **Yuwei Li:** Software, Resources. **Qianqian Liu:** Software, Formal analysis. **Jian Zhang:** Investigation. **Jifang Liu:** Supervision, Funding acquisition. **Shisong Han:** Supervision, Conceptualization. **Bin Yang:** Writing – review & editing, Supervision, Project administration, Methodology, Funding acquisition, Conceptualization.

Acknowledgments

This research was supported by the National Key R&D Program of China (No. 2022YFC2304205), National Natural Science Foundation of China (Nos. 51903062, 52273128) and the Plan on Enhancing Scientific Research in GMU (No. 02-410-2405033).

Supplementary materials

Supplementary material associated with this article can be found, in the online version, at doi:10.1016/j.cclet.2024.110437.

References

[1] S.J. Dixon, K.M. Lemberg, M.R. Lamprecht, et al., Cell 149 (2012) 1060–1072.
[2] X. Jiang, B.R. Stockwell, M. Conrad, Nat. Rev. Mol. Cell Biol. 22 (2021) 266–282.
[3] X. Chen, C. Yu, R. Kang, et al., Cell Death Differ. 28 (2021) 1135–1148.
[4] W.S. Yang, R. SriRamaratnam, M.E. Welsch, et al., Cell 156 (2014) 317–331.
[5] Y. Zou, H. Li, E.T. Graham, et al., Nat. Chem. Biol. 16 (2020) 302–309.
[6] H. He, L. Du, H. Xue, et al., Small Methods 7 (2023) 2300230.
[7] X. Yu, T. Shang, G. Zheng, et al., Chin. Chem. Lett. 33 (2022) 1895–1900.
[8] X. Chen, R. Kang, G. Kroemer, et al., Nat. Rev. Clin. Oncol. 18 (2021) 280–296.
[9] W. Wang, M. Green, J.E. Choi, et al., Nature 569 (2019) 270–274.
[10] T. Shang, X. Yu, S. Han, et al., Biomater. Sci. 8 (2020) 5241–5259.
[11] J. Huang, B. Yang, Y. Peng, et al., Adv. Funct. Mater. 31 (2021) 2011171.
[12] T. Nie, H. Liu, Z. Fang, et al., ACS Nano 17 (2023) 10925–10937.
[13] Y. Li, Y. Duan, Y. Li, et al., Exploration 5 (2025) 20230117.
[14] Y. Wu, Z. Zhang, Y. Wei, et al., Chin. Chem. Lett. 34 (2023) 108098.
[15] L. Sun, J. Wu, F. Du, et al., Science 339 (2013) 786–791.
[16] L. Corrales, L.H. Glickman, et al., Cell Rep. 11 (2015) 1018–1130.
[17] T.F. Gajewski, E.F. Higgs, Science 369 (2020) 921–922.
[18] C. Wang, Y. Guan, M. Lv, et al., Immunity 48 (2018) 675–687.
[19] L. Cao, H. Tian, M. Fang, et al., Biomaterials 290 (2022) 121856.
[20] H. Tian, G. Wang, W. Sang, et al., Nano Today 43 (2022) 101405.
[21] H. Dai, Q. Fan, C. Wang, Exploration 2 (2022) 20210157.
[22] X. Yang, Y. Yang, J. Bian, et al., Nano Today 38 (2021) 101109.
[23] Y. Li, J. Cui, C. Li, et al., Chin. Chem. Lett. 34 (2023) 108180.
[24] H. He, L. Du, M. Tan, et al., Sci. China Chem. 63 (2020) 936–945.
[25] Y. Zhuang, S. Han, Y. Fang, et al., Coordin. Chem. Rev. 455 (2022) 214360.
[26] S. Wang, R. Ma, Z. Mei, et al., Med. Mat 1 (2024) 6–26.
[27] M. Zhou, X. Wang, S. Lin, et al., Adv. Healthc. Mater. 9 (2020) 2000064.
[28] H. Zhang, T. Wang, Y. Zheng, et al., Biochem. Biophys. Res. Commun. 499 (2018) 488–492.
[29] Q. Jiang, L. Fan, J. Sun, et al., ACS Mater. Lett. 3 (2021) 1778–1785.
[30] L. Xie, G. Wang, W. Sang, et al., Biomaterials 269 (2021) 120638.
[31] L. Xu, M. Peng, T. Gao, et al., Adv. Sci. 11 (2024) 2306203.
[32] N. Han, L.G. Li, X.C. Peng, et al., Eur. J. Pharmacol. 919 (2022) 174797.
[33] J. Jiang, X. Cui, Y. Huang, et al., Nano Biomed. Eng. 16 (2024) 152–187.
[34] L. Xu, Y. Liu, X. Chen, et al., Biomed. Pharmacother. 159 (2023) 114241.
[35] Q. Liu, X. Chen, Y. Jiang, et al., Adv. Funct. Mater. 34 (2024) 2311677.
[36] T. Shang, X. Yu, Y. Gu, et al., Int. J. Biol. Macromol. 251 (2023) 126539.
[37] H. Zhu, K. Ma, R. Ruan, et al., Chin. Chem. Lett. 35 (2024) 108536.
[38] G. Wang, J. Yan, H. Tian, et al., Adv. Mater. 36 (2024) 2312588.
[39] J. Yan, G. Wang, L. Xie, et al., Adv. Mater. 34 (2022) 2105783.
[40] C. Chen, Y. Tong, Y. Zheng, et al., Small 17 (2021) 2006970.
[41] Y. Wang, M. Wu, X. Wang, et al., Mater. Today Bio 18 (2022) 100531.